

Self-Patterning of Multifunctional Heusler Membranes by Dewetting

Klara Lünser,* Anett Diestel, Kornelius Nielsch, and Sebastian Fähler

Ni-Mn-based Heusler alloys are an emerging class of materials which enable actuation by (magnetic) shape memory effects, magnetocaloric cooling, and thermomagnetic energy harvesting. Multifunctional materials have a particular advantage for miniaturization since their functionality is already built within the material. However, often complex microtechnological processing is required to bring these materials into shape. Here, self-organized formation of single crystalline membranes having arrays of rectangular holes with high aspect ratio is demonstrated. Dewetting avoids the need for complicated processing and allows to prepare freestanding Ni-Mn-Ga-Co membranes. These membranes are martensitic and magnetic, and their functional properties are not disturbed by self-patterning. Feature sizes of these membranes can be tailored by film thickness and heat treatment, and the tendencies can be explained with dewetting. As an outlook, the advantages of these multifunctional membranes for magnetocaloric and thermomagnetic microsystems are sketched.

1. Introduction

Ni-Mn-based Heusler alloys are multifunctional materials that exhibit magnetic and martensitic transformations. The combination of both transformations enables various applications: These alloys can be used for actuation either with temperature using the conventional shape memory effect,^[1] or with a magnetic field using magnetically induced reorientation,^[2] which enables strains up to 12%.^[3] Furthermore, Ni-Mn-based Heusler alloys have outstanding properties for magnetocaloric refrigeration^[4] and for thermomagnetic harvesting of low-grade

waste heat.^[5,6] To optimize the Heusler alloys for each of those applications, the magnetic and martensitic transformation can be tuned by adjusting the composition^[1] and alloying.^[7-9]

Heusler alloys can be produced as thin films to integrate these applications into microsystems. The reduced size of microsystems not only opens new application possibilities, but can also increase the efficiency of the systems. For magnetocaloric refrigeration,^[10] thermomagnetic harvesting,^[6] and shape memory actuators,^[11] the key benefit is the accelerated heat exchange due to the high surface to volume ratio, which allows for faster cycles and thus higher power densities. For magnetic shape memory (MSM), microactuators promise a high

stroke, without the complications of an additional lever.^[12] In particular, MSM microactuation requires single crystalline films.^[13] But since polycrystalline Heusler alloys tend to be brittle,^[14] also the other applications benefit from the absence of grain boundaries. For all microsystems, freestanding films are required because a substrate hinders a macroscopic elongation and represents an unfavorable heat sink. Microtechnological systems usually need to be fabricated in specific shapes or geometries. This requires microtechnological processing after the film deposition. However, these chemically ordered Heusler alloys are a challenge for microtechnological processing.^[12,15-17] A particular problem is the damage caused by ion beam methods, because this damage needs to be removed afterward.^[18] This processing could be minimized if the multifunctional material brought itself into the desired shape through self-patterning. Up to now, only one approach for self-patterned Heusler films is known: by exploiting the lattice mismatch between the Ni-Mn-Ga film and the MgO substrate, a self-patterned surface of (110)-oriented crystals on top of a (001)-oriented film was produced.^[19] This surface layer only forms at a high mismatch between substrate and film and when a certain thickness is reached. To address the needs of multifunctional microsystems, however, more dedicated patterns are required.

A self-patterning process that is mostly, but not exclusively, used for single element films such as gold or silicon, is dewetting.^[20,21] During dewetting, a smooth and continuous film is heated up, which first results in holes through the film and finally leads to a morphology of isolated island arrays.^[22] The temperatures needed can be well below the film's melting temperature, which means that the film remains solid throughout the process. The underlying driving force is the minimization

K. Lünser, A. Diestel, K. Nielsch, S. Fähler
Leibniz IFW Dresden
Institute for Metallic Materials
01069 Dresden, Germany
E-mail: k.luenser@ifw-dresden.de

K. Lünser, K. Nielsch
TU Dresden
Institute of Materials Science
01062 Dresden, Germany

K. Nielsch, S. Fähler
TU Dresden
Institute of Applied Physics
01062 Dresden, Germany

 The ORCID identification number(s) for the author(s) of this article can be found under <https://doi.org/10.1002/admi.202100966>.

© 2021 The Authors. Advanced Materials Interfaces published by Wiley-VCH GmbH. This is an open access article under the terms of the Creative Commons Attribution-NonCommercial License, which permits use, distribution and reproduction in any medium, provided the original work is properly cited and is not used for commercial purposes.

DOI: 10.1002/admi.202100966

of the total surface energy. Film thickness, temperature, and annealing time are the key parameters controlling dewetting.^[21]

Here, we combine dewetting with multifunctional Heusler alloys to obtain freestanding films that exhibit holes with high aspect ratios. We demonstrate that, at appropriate growth conditions, one can obtain Ni–Mn–Ga–Co membranes, which are single crystalline. In the first part of this paper, we examine the morphology and functional magnetic and martensitic properties of one particular membrane in detail and show that neither its martensitic nor magnetic microstructure is disturbed by self-patterning. In the second part, we analyze how deposition temperature, thickness, and an additional heat treatment can be used to tailor the hole morphology. Thus, it is possible to customize the film as needed for applications. Our observations show that the formation of the holes can be explained by the concept of dewetting, which has been reported for other materials. Within the outlook, we describe two microsystem applications, which could be enabled by our multifunctional membranes.

2. Results

Starting point is the morphology and the functional properties of one Ni–Mn–Ga–Co film that grows with self-patterned, faceted holes. For this analysis, we chose an 800 nm thick epitaxial Ni₄₉Mn₁₈Ga₂₄Co₉ film grown with sputter deposition on MgO(001) at a deposition temperature of 600 °C. The film's microstructure is shown in **Figure 1**, which includes an overview of the freestanding, martensitic membrane in **Figure 1a**. As some measurements were conducted with the film still attached to the substrate, in the following, we call the samples “membrane” only when we mean the freestanding version of the film. The film top view in **Figure 1b** reveals two distinct features of this film: the self-patterned holes and the martensitic microstructure. The martensitic microstructure is evident from the striped contrast that runs in a 45°-angle to the micrograph edges.^[23] This channeling contrast is caused by martensitic variants of different orientations. As second feature, the self-patterned holes are visible as dark regions. Most of the holes are rectangular and seem to narrow towards the bottom of the hole. By peeling the films from the substrate, the bottom side was imaged as well (**Figure 1c**). The holes on the bottom side are also mainly rectangular but smaller than on the top. Most of the rectangular holes on both sides are aligned in A[100] and A[010] direction (for simplicity, we describe crystallographic orientations in the austenitic coordinate system (A), even though the film is martensitic at room temperature). A statistical analysis of several SEM images quantified that the top side is covered with 3.5 holes per μm² on average. In contrast, the bottom side shows 0.8 holes per μm², which means that approximately 23% of the holes penetrate the complete film thickness. A film cross section prepared by focused ion beam (FIB, **Figure 1d**) completes the analysis of the holes. Like a funnel, the holes edges are perpendicular to the substrate and film surface, while the corners on the top side are sloped in a 45°-angle. The epitaxial growth allows to assign the perpendicular planes to A(100) and A(010), while the inclined planes at the top belong to the A{110}-plane family. With an average hole size of 0.8 × 10⁻² μm²

on the bottom side of the membrane, the average hole width is 90 nm. The aspect ratio, defined as the ratio of the film thickness and the average hole width, is around 9:1. Apart from the holes, the microstructure looks very typical for martensitic, epitaxial Ni–Mn-based Heusler films on MgO(001). Both, the top view and the cross section, show two characteristic martensitic microstructures called Type X and Type Y^[23,24] with twin boundaries on different length scales. In the cross section, branching of the twin boundaries is visible near the substrate. The martensitic variants on the bottom side of the membrane are therefore too small to see in **Figure 1c**.

Information about the functional properties can be drawn from the structural and magnetic measurements in **Figure 2**. To analyze the crystal structure of the film, we measured diffractograms in Bragg–Brentano geometry at offset angles from 0° to 10°. The offset angles are important to measure planes of the martensite, which are slightly tilted away from the surface in epitaxial films.^[25] The respective measurements were summed up in **Figure 2a**. The measured intensities are compared with reflex positions for the austenite, non-modulated martensite (NM), and 14M modulated martensite, which were calculated using bulk lattice parameters of Ni–Mn–Ga–Co.^[7] Apparently, most of the sample is martensitic. The M(202)-pole figure in **Figure 2b** allows a similar conclusion because it agrees well with its calculated counterpart (**Figure 2b**, lower half). As the pole figure was calculated assuming an epitaxy relation of MgO(001) [100] || Ni–Mn–Ga–Co(001)_A [110]_A, we can confirm that the film grows in this relation, which is well known for Ni–Mn–X-films.^[10,25–27] To summarize, the diffraction experiments reveal that the sample is martensitic at room temperature and accordingly that the martensitic transformation must occur at higher temperatures.

Using magnetization measurements at external magnetic fields of 0.1 and 2 T, we measured the magnetic transformation behavior of the film. From the measurements in low fields, we obtain a Curie temperature of 347 K, which means that the sample is magnetic at room temperature. No discontinuity is observed in the magnetization curves, which would be characteristic for a martensitic transformation. Consequently, we conclude that the martensitic transformation occurs above the Curie temperature.

SEM micrographs and pole figure measurements indicate that the martensite is not disturbed by the holes and that it grows similar, if not identical, to martensite in films without self-patterning.^[24] To further evaluate this hypothesis, we examined the film with atomic force microscopy (AFM) and magnetic force microscopy (MFM) in **Figure 3**. The martensitic microstructure and the holes are visible in the AFM image (**Figure 3a**). With a maximum height of 350 nm, none of the holes seems to reach down to the substrate. This, however, is an artifact because the pyramidal AFM tip cannot reach the bottom of the holes. The profile in **Figure 3c** shows the typical height profile of Type X 14M martensite,^[28] which is not well visible in the AFM image due to the large contrast from the deep holes. Not only does the AFM image hint that the martensitic microstructure is undisturbed by the holes, but also the MFM image in **Figure 3b** shows the typical magnetic domain pattern of Type X.^[29]

The domain pattern is aligned perpendicular to the striped pattern of the martensitic twin boundaries. Occasional

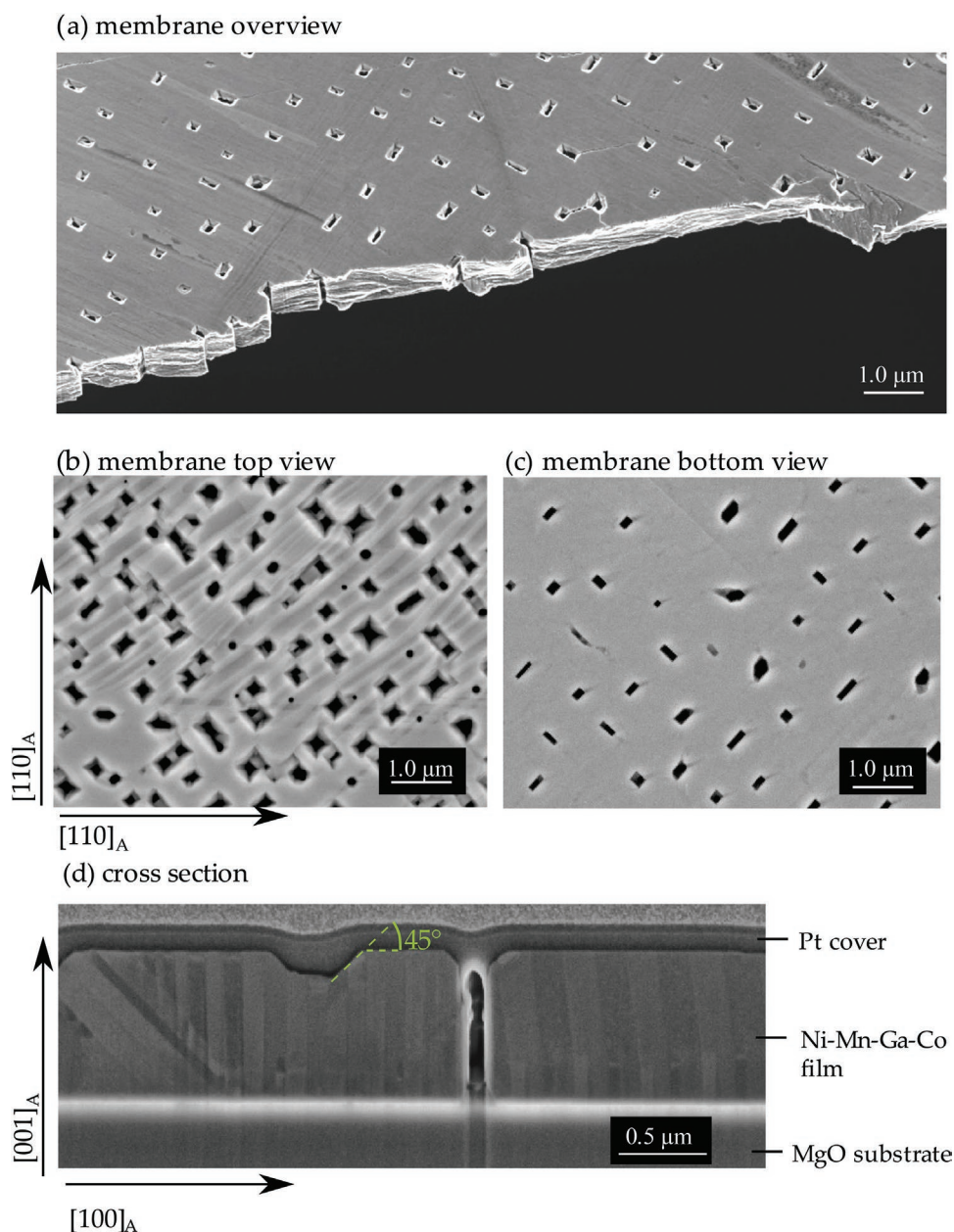


Figure 1. SEM images showing the microstructure of an 800 nm thick membrane prepared at a deposition temperature of 600 °C. a) Inclined view of the peeled-off and cracked membrane. b) Film top side (backscattered electron contrast). The film surface is covered with holes that formed during deposition. The holes mostly have a rectangular cross section along the A[100] and A[010] directions. The striped contrast in the upper half of the image comes from the martensitic microstructure (Type X). c) The film's bottom side shows fewer and smaller rectangular holes than the top side. d) FIB cross section of the funnel-shaped holes with corners that are inclined by 45°. Some of the holes, which are cut directly by FIB, penetrate the complete film.

switches in the magnetization contrast can be attributed to mirroring variant boundaries.^[29] Two of these boundaries are marked with arrows in Figure 3b. The striped contrast in the darker domains coincides with the topography contrast in the AFM micrograph. It occurs because some topography contrast was measured during the magnetic measurement as well. To evaluate if the holes change the magnetic domain pattern, we overlaid the MFM image with outlines of the holes. It becomes obvious that not only the martensitic microstructure, but also the magnetic domain pattern is undisturbed by the

holes. Moreover, our results show that the magnetic domain pattern of Ni–Mn–Ga–Co does not differ from the one reported for Ni–Mn–Ga.^[29]

Combining these results, we obtain a freestanding single crystalline membrane with martensitic and magnetic transitions above room temperature and with many rectangular, funnel-like holes. Neither the martensitic nor the magnetic microstructure is affected by the hole pattern, which indicates that the functional properties are not disturbed by self-patterning.

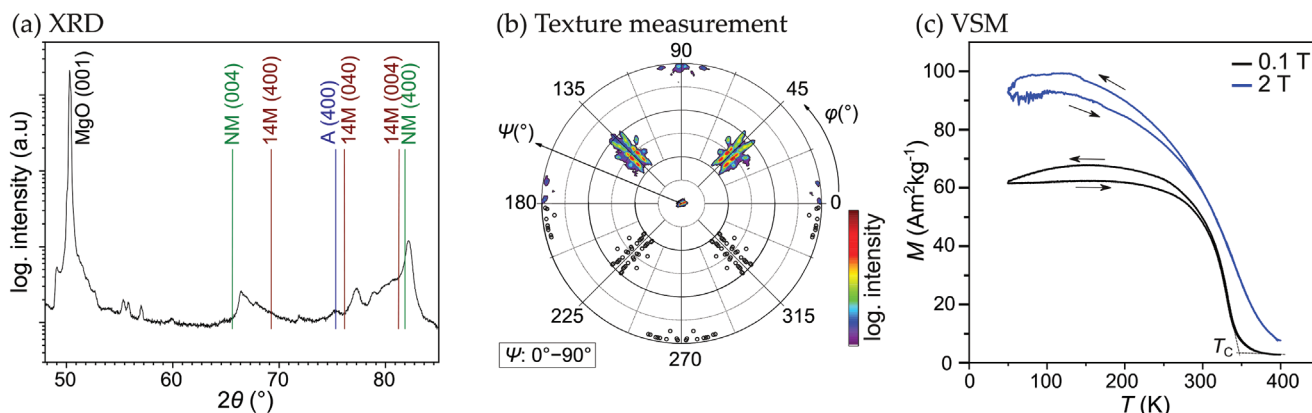


Figure 2. Structural and magnetic properties of the 800 nm thick $\text{Ni}_{49}\text{Mn}_{18}\text{Ga}_{24}\text{Co}_9$ film ($T_{\text{Dep}} = 600\text{ }^\circ\text{C}$): a) Summed up XRD-diffractograms taken in Bragg–Brentano geometry with offset angles from 0° to 10° show that the film is martensitic at room temperature. The reflex positions are calculated using the lattice parameters for Ni–Mn–Ga–Co from.^[7] b) Measured (top half) and calculated (lower half) $M(202)$ -pole figure match up well and reveal the (001)-oriented epitaxy of the film. c) $M(T)$ -measurements at external magnetic fields of 0.1 and 2 T. The Curie temperature T_C of 347 K is determined using tangents to the curves. Arrows represent the measurement direction.

2.1. Tailoring Membrane Properties by Deposition Conditions and Additional Heat Treatment

In the previous section, we demonstrated that our membranes have the required multifunctional properties; here we analyze how the morphology can be tailored by deposition temperature, film thickness, and annealing conditions. Furthermore, we will use these experiments within the discussion to show that dewetting is the relevant self-patterning process. The deposition conditions and characteristic values for the hole morphologies are summarized in **Table 1**.

To analyze the influence of the deposition temperature, we prepared 800 nm thick films at 400, 500, and 600 $^\circ\text{C}$, summarized in **Figure 4**. The SEM images of the films show representative regions of the film microstructure. Using MATLAB image analysis of several additional micrographs, we calculated

the average hole size, the number of holes per area, and the hole coverage in percent. Because the film composition (see **Table 1**) and chemical ordering changes with rising deposition temperatures, the films have different martensitic transition temperatures. That is why the film deposited at 600 $^\circ\text{C}$ shows the typical martensitic microstructure, whereas the films deposited at 400 and 500 $^\circ\text{C}$ are austenitic. This conclusion is drawn from the surface morphology and is confirmed with corresponding XRD measurements (see **Figure S1**, Supporting Information). The microstructure of the 400 $^\circ\text{C}$ film is characterized by some terraces that occur during growth and by small, but numerous holes (for an enlarged image, see **Figure S2**, Supporting Information). In comparison, the 500 $^\circ\text{C}$ film shows fewer and larger holes. The SEM image of the 600 $^\circ\text{C}$ film was already described in the previous section. Again, the holes are larger and fewer in number. In summary, with rising

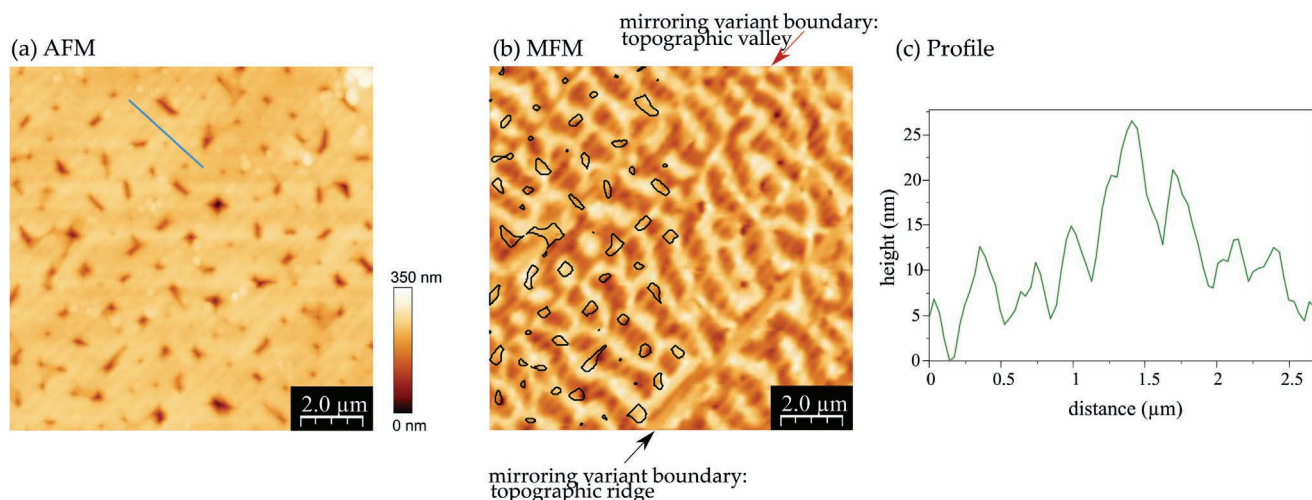


Figure 3. Surface topography and magnetic domain analysis of the 800 nm thick film grown at 600 $^\circ\text{C}$: a) AFM image with color-coded height contrast. b) MFM image. The AFM and MFM images are taken simultaneously in the same sample region. The left half of the MFM image is overlaid with the outlines of the holes from (a). Two mirroring variant boundaries in the MFM image are marked with arrows. c) Height profile along the blue line marked in (a) reveals the typical sawtooth height profile of Type X martensite.

Table 1. Summary of deposition conditions for films prepared at different deposition temperatures and thicknesses. If applicable, subsequent annealing is specified as well. The holes are analyzed using image analysis in MATLAB to calculate characteristic values for the films.

Composition [at.%]	Deposition temperature [°C]	Film thickness [nm]	Deposition time [min]	Annealing	Average no. of holes per μm^2	Average hole size [μm^2]	Hole area [%]
$\text{Ni}_{49}\text{Mn}_{18}\text{Ga}_{24}\text{Co}_9$	600	800	81	–	3.5	4.2×10^{-2}	13.2
$\text{Ni}_{45}\text{Mn}_{27}\text{Ga}_{21}\text{Co}_7$	500	800	81	–	12.1	5.3×10^{-3}	6.0
$\text{Ni}_{44}\text{Mn}_{28}\text{Ga}_{21}\text{Co}_7$	400	800	81	–	62.1	5.1×10^{-4}	2.7
$\text{Ni}_{48}\text{Mn}_{20}\text{Ga}_{23}\text{Co}_9$	600	400	43	–	7.0	1.8×10^{-2}	12.3
$\text{Ni}_{47}\text{Mn}_{19}\text{Ga}_{25}\text{Co}_9$	600	80	8	–	1.9	8.1×10^{-2}	14.9
$\text{Ni}_{53}\text{Mn}_8\text{Ga}_{30}\text{Co}_9$	600	80	8	600 °C, 35 min	1.9	1.5×10^{-1}	29.1

deposition temperature, the hole size increases, whereas the total number of holes decreases. The hole size histograms visualize an additional trend: with higher deposition temperatures, the hole size scatters more. This implies that some holes grow more than others as the deposition temperature rises. Regardless of the deposition temperature, the holes edges are mostly rectangular, and oriented in A[100] and A[010] direction.

In addition to the deposition temperature, we analyzed the effect of the film thickness on the self-patterning using films of 80, 400, and 800 nm thickness deposited at 600 °C. Figure 5a–c shows how the appearance of the holes changes with increasing film thickness. The 80 nm thick film (Figure 5a) has irregularly shaped holes that look worm-like or oval. The holes do not show the rectangular shapes that are present in the thicker film. Nevertheless, some of the worm-like features are oriented at a 45° angle with respect to the substrate edges. The 80 nm film does not show any signs of martensitic microstructure, it appears to be austenitic at room temperature. On the 400 and 800 nm thick films, however, the characteristic stripy

martensitic microstructure of Type X is visible. The distance between the stripes is larger for the 800 nm thick film than for the 400 nm thick film, which is a common feature in epitaxial films: In thicker films, martensitic nuclei can grow larger before their growth is restricted by the substrate.^[30] The self-patterning changes also with increasing film thickness: the 400 nm film contains more, but smaller holes compared to the 80 and 800 nm thick films. The number of holes decreases from 400 to 800 nm because holes grow together. One example is indicated in red in Figure 5c. The areal hole fraction, however, stays roughly constant for all three films Figure 5a–c.

A further possibility to control the self-patterning is an additional annealing treatment. Figure 5a,d compares two 80 nm thick films, one without annealing and one with an additional annealing at 600 °C for 35 min directly after deposition. Whereas the unannealed film shows worm-like holes, the holes are rectangular after annealing. Like the 400 and 800 nm thick film, the annealed film shows the funnel-like shapes that arise from the formation of {110}-oriented facets. For the 80 nm thick

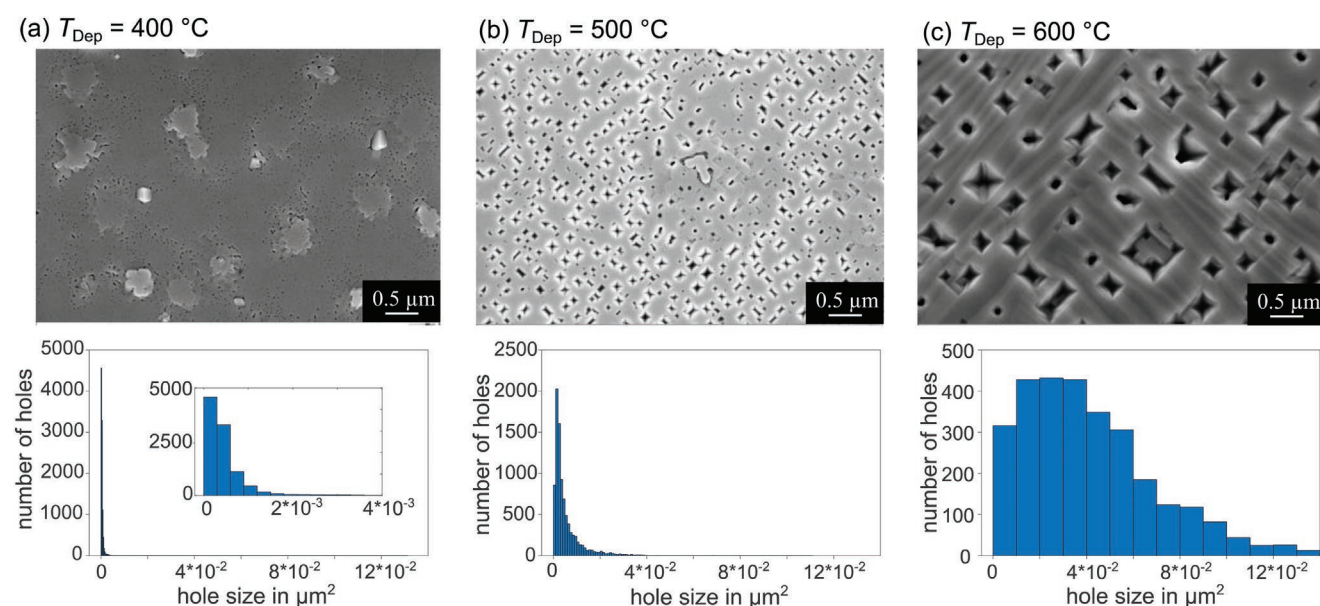


Figure 4. The microstructure and self-patterning of the films change with the deposition temperature. a–c) SEM images and histograms of hole sizes of films after a deposition at temperatures of 400, 500, and 600 °C. The histograms of the hole size in μm^2 show that the size of an average hole and the scatter of the hole size increase with rising deposition temperature. In contrast, the total number of holes per μm^2 decreases. For better comparability, the x-axis of the histograms is kept constant for all films. The inset in (a) therefore shows the hole size distribution of the 400 °C film in more detail.

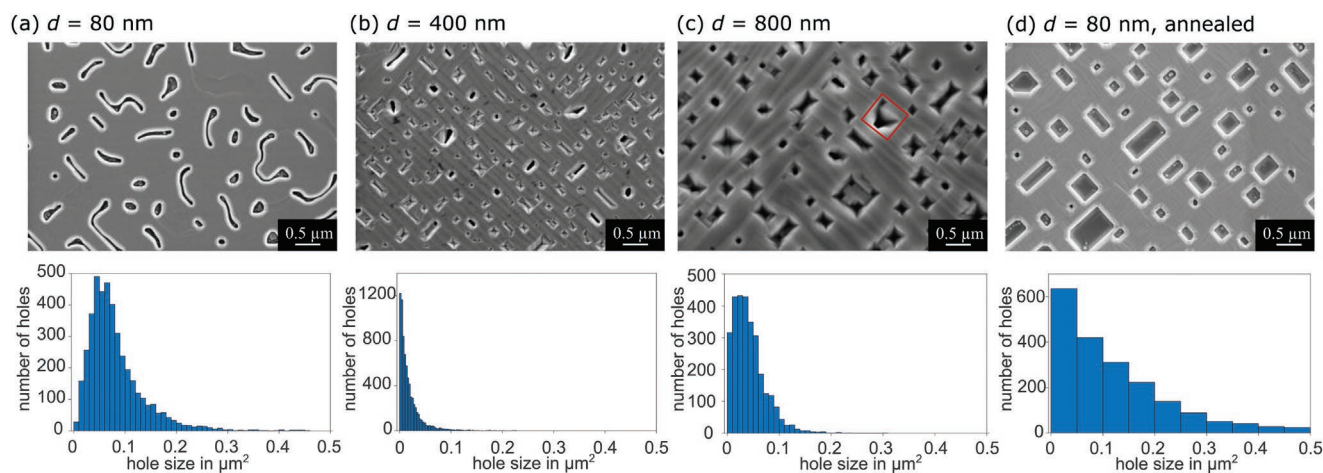


Figure 5. The microstructure and self-patterning of the films change with film thickness and additional annealing. a–c) SEM images of films with a film thickness d of 80, 400, and 800 nm. d) SEM image of an 80 nm thick film that is annealed at 600 °C for 35 min after annealing. All films are deposited at 600 °C. The respective histograms of the hole size show that the size of an average hole decreases from 80 to 400 nm thickness and increases again for the 800 nm thick film. Annealing increases the average hole size. The red square in (c) marks a region where several holes have grown together.

film, the deposition time of 8 min is comparably short, therefore, the film is only exposed to high temperatures for a short amount of time. Apparently, this time is not sufficient to fully develop the funnel-like rectangle shapes. The average number of holes is not changed by the annealing; however, the average hole size rises from 0.08 to 0.15 holes per μm^2 , indicating that the holes grow in size.

The SEM micrograph of the 80 nm thick, annealed film (Figure 6) shows the microstructure in more detail. The small stripy contrast indicates that the film is martensitic at room temperature, although the unannealed film was austenitic (for complementary XRD data, see Figure S1, Supporting Information). This might either come from composition changes during annealing or because the annealing enhances the chemical order. The martensitic microstructure of this film is interrupted by the holes. This contrasts with the 800 nm thick film, where the martensite grows mainly undisturbed by the holes. The effect can be explained with the different hole morphology

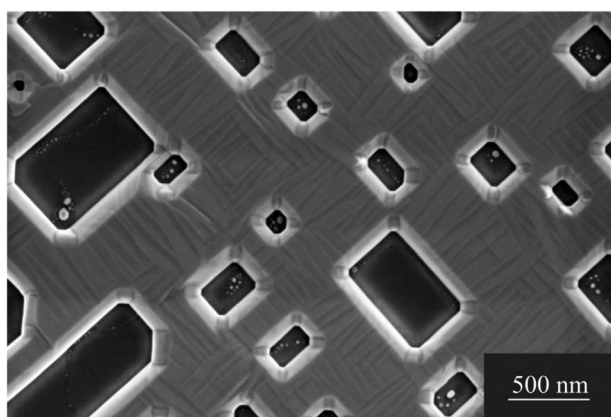


Figure 6. SEM micrograph of the 80 nm thick, annealed film (T_{Dep} : 600 °C, annealing for 35 min). For this film, the martensitic microstructure must adapt to the holes, because the holes are large compared to the size of the martensitic variants. Nevertheless, the martensitic microstructure resembles the typical Type X microstructure.

of the thin film: The holes here are three times larger and cover twice the area. The small martensitic variants, therefore, do not have enough undisturbed material to grow continuously. Nevertheless, the martensitic microstructure resembles the typical Type X microstructure that was observed in the other films as well.

Our results show that the shape, size, and number of holes are customizable by changing deposition temperature, film thickness, and heat treatment.

3. Discussion

We propose that the hole arrays originate from dewetting. This concept is known to produce holes in metallic films of, for example, Fe, Ni, or Au^[31–33] and occurs because dewetting minimizes the total surface energies of the film and the film-substrate interface.^[22] We can explain our experiments by looking at three particular interface energies for Ni-Mn-Ga-Co: The surface energy of {001} planes, the surface energy of {110} planes, and the film-substrate interface energy. To compare the surface energies of the planes, we consider that Heusler alloys are bcc structured when neglecting the chemical ordering. In bcc structures, the {110} planes have been calculated as the planes of lowest surface energy.^[34] Indeed, most polycrystalline Ni–Mn-based Heusler films are (110)-textured,^[35] or reach a (110)-texture after annealing.^[36] Moreover, this orientation is sometimes observed with increasing film thickness in originally (001)-oriented films.^[19] We expect that {100} planes exhibit a slightly higher energy, but during epitaxial growth on MgO(001) this orientation is induced by the substrate orientation with identical symmetry. Of highest energy is the interface energy between the Heusler alloy and the oxidic substrate. The minimization of this energetically unfavorable interface drives the dewetting because more holes mean less interface. Consequently, we observe that with increasing temperature and annealing time the fraction of hole area increases. In addition, the holes become larger, which reduces the total area of their

surrounding {100} planes. In our experiments, the holes additionally form well-defined funnel shapes, which consist of low energy {110} planes. We predict that for much longer annealing times these planes will dominate and thus a morphology of faceted islands will form. However, the difference between {100} and {110} surfaces energies seems to be low, which gives a large process window for metastable hole arrays.

In addition to these thermodynamic arguments, kinetics is decisive for dewetting. Dewetting mostly nucleates at defects and the films include several types of defects that might be relevant: the films exhibit dislocations and small-angle grain boundaries, which arise during initial film growth when islands with small inclinations coalesce. Small facets or terraces on the MgO substrates might have an influence as well.^[37] Moreover, dewetting is also known to take place at vacancies. In our films, vacancies arise because Mn, which has a high vapor pressure, evaporates substantially at high temperatures. Lastly, the films grow with a certain epitaxial misfit and therefore with a certain strain.^[38] Possibly, when the films are under tension in plane, the tension is relaxed by the formation of the holes.^[39]

Dewetting is a process driven by diffusion, therefore it requires temperature and time. This explains why we observed an increase in hole size with higher temperatures. It can also clarify the difference in hole morphology originating from the additional annealing of the 80 nm film. With a deposition time of only 8 min, the time for diffusion is limited. Only the additional annealing offers enough time to form the low energy {100} or {110} facets. With more time, some holes grow larger at the expense of smaller holes, a process that is known as Ostwald ripening. Therefore, the hole number decreases with rising temperature and film thickness. In short, all observed trends can be explained well with the thermodynamic and kinetic concepts of dewetting.

SEM, AFM, and MFM micrographs of the thick film reveal that neither the martensitic microstructure nor the domain pattern is influenced by self-patterning. This indicates that the self-patterning process does not disturb the functional material in vicinity of the pattern, which is often a problem during top-down approaches—in particular when patterning ratios. As the holes form within the austenitic state at high deposition temperatures, the martensitic microstructure forms later and thus does not affect the hole pattern. Also, the hole pattern does not affect the martensitic microstructure. This observation agrees with our recent explanation of the hierarchically twinned martensite, which leaves hardly any freedom to change the martensitic microstructure.^[24] Only for the 80 nm thin postannealed film we observe a slight change of the martensitic microstructure, which we attribute to the very large areal fraction of the holes. Finally, also the magnetic microstructure remains unchanged. The magnetic domain pattern within the martensitic state is mostly governed by minimizing anisotropy energy and stray fields and therefore adapts to the martensitic microstructure.^[29] As this microstructure remains unaffected, the same is expected for the magnetic domain pattern. However, differences due to stray fields in vicinity of the holes are possible, but they are below the resolution of our MFM measurements. Thus, self-patterning through dewetting provides a way to produce patterned Heusler thin films without disturbing the martensitic and magnetic microstructure and the functional properties.

4. Conclusion

Multifunctional membranes with hole arrays were produced by adapting the dewetting process to Heusler alloys. We obtain Ni–Mn–Ga–Co membranes that are magnetic as well as martensitic, and their martensitic and magnetic microstructures are not disturbed by self-patterning. Appearance, size, and density of holes can be tailored by deposition temperature, film thickness, and annealing procedures. Holes studied here reach a high aspect ratio of up to 9:1 and areal densities of 29%. Our approach is versatile as the resulting multifunctional membranes are single crystalline and freestanding, which is required for most microsystem applications of Heusler alloys.

There are two particular applications, which benefit from nothing but holes. The first application is magnetocaloric refrigeration, which recently saw a boost by the use of heat pipes.^[40] To downscale this bulk approach for microsystems with increased cycle frequency, we propose to use our freestanding membranes. The holes would allow the gaseous media that serves as the heat transport medium to travel from one chamber to the next one. The second application is thermomagnetic harvesting, where microsystems benefit from faster heat exchange.^[6] For further improvement, we propose to fill the holes in our membranes with copper using electroplating. Cu exhibits a heat conductivity of $386 \text{ WK}^{-1} \text{ m}^{-1}$,^[41] which is much higher than the $15.6 \text{ WK}^{-1} \text{ m}^{-1}$ of Heusler alloys.^[42] Accordingly, Cu represents a fast track for heat exchange throughout the film. For this increase of cycle frequency, it is neither required that all holes penetrate the complete film nor that the films are freestanding. Consequently, it will be possible to use thin membranes on the thermally insulating MgO substrate. Both applications benefit from the high aspect ratio of the holes, while certain variations of their arrangement and size, which are typical for self-patterning, are no disadvantage. However, both applications will require further optimization of our membranes. Especially the different temperatures used in both applications require that the membrane's magnetic and martensitic transformation temperatures are adapted by adjusting the composition.

5. Experimental Section

The well-established epitaxial growth of Heusler films on heated single crystalline (001)-oriented MgO substrates allows to prepare the thin film counterpart of single crystals.^[25–27] The authors use DC magnetron sputter deposition from an alloyed $\text{Ni}_{44}\text{Mn}_{32}\text{Ga}_{24}$ and an elemental Co-target to deposit the Ni–Mn–Ga–Co system, which exhibits promising magnetocaloric properties.^[43] The sputtering chamber has a base pressure of 1×10^{-9} mbar, while sputtering took place at 8×10^{-3} mbar with an Ar–H mixture (5 vol.% H) as sputter gas. During deposition, the substrates were rotated for homogenous thickness and composition, and heated to temperatures ranging from 400 to 600 °C required for epitaxial growth. Films were deposited with various deposition temperatures and thicknesses; their deposition conditions are summarized in Table 1. One film was heat-treated in the sputtering chamber directly after deposition. The chemical composition of the films was determined with energy-dispersive X-ray spectroscopy on a JEOL JSM-6510 scanning electron microscope with an accuracy of 1 at.%. It was observed that with higher deposition temperatures, the Mn-content within the films decreases. This can be attributed to the vaporization

pressure of Mn, which increases strongly with rising temperatures.^[44] A film cross section was prepared with FIB with an FEI Helios NanoLab 600i. The contrast of the FIB image in Figure 1d was adapted using contrast-limited adaptive histogram equalization to enhance the visibility of the martensitic variants.

The film's crystal structure was analyzed on the substrate-constraint films with a Bruker D8 X-ray Diffractometer using Co-K α radiation of $\lambda = 0.178997$ nm. 2θ ranging from 20° to 100° was measured with a step size of 0.02° and 1 s step^{-1} . To probe martensite as well as austenite, regular Bragg–Brentano geometry (θ – 2θ) was insufficient, because it cannot detect the slightly tilted martensitic planes.^[25] Therefore, the geometry was adapted to ω – 2θ using offsets of $\Delta\omega = \omega - \theta$ ranging from 0° to 10° . The measurements for all $\Delta\omega$ angles were then summed up. The epitaxial relationship between film and substrate was determined with pole figures in four-circle setup using a Philips X'Pert four-circle-diffractometer with Cu-K α radiation of $\lambda = 0.15406$ nm. The tilting angles Ψ and ϕ were measured in steps of 1° , respectively. The pole figure was calculated using the nonlinear elasticity-based continuum mechanics as described by Bhattacharya^[45] with MATLAB code adapted from.^[24] The adapted code can be found in the Supporting Information.

SEM micrographs were taken with a ZEISS LEO 1530 Gemini microscope. To image the bottom side of the samples, the film was peeled off the substrate.^[46] The micrographs were used to determine the hole size, number, and area using image analysis in MATLAB. For reasonable statistics, at least 2000 holes were measured for size, and holes were counted in an area of at least $4000 \mu\text{m}^2$.

The magnetization as a function of temperature was measured in a physical properties measurement system with a vibrating sample magnetometry option. For the measurement, a constant magnetic field was applied in plane and the sample was heated up to 400 K before being cooled down and heated up at a constant cooling/heating rate of 3 K min^{-1} .

The martensitic and magnetic microstructures were analyzed with AFM and MFM using an ICON AFM (Bruker). The height contrast in tapping mode was used to image the topography and the lift mode with a standard magnetic tip for the magnetic micrographs. The tip was magnetized along the tip axis and the lift scan height was set to 100 nm. AFM and MFM micrographs were analyzed using WSxM.^[47] All picture edges and pole figures in this paper were in parallel to MgO[100] and MgO[010], which corresponds to austenite A[110] and A[$\bar{1}$ 10].

Supporting Information

Supporting Information is available from the Wiley Online Library or from the author.

Acknowledgements

This research was funded by DFG via Priority Program SPP 1599 (FA 453/11) and project FA 453/14. The authors acknowledge J. Scheiter for performing the FIB cut and Y. Ge, S. Schwabe and M. Kohl for helpful discussion.

Open access funding enabled and organized by Projekt DEAL.

Conflict of Interest

The authors declare no conflict of interest.

Data Availability Statement

The data that support the findings of this study are available from the corresponding author upon reasonable request.

Keywords

epitaxial films, Heusler alloys, magnetic domain structure, martensite, Ni–Mn–Ga–Co, self-patterned Heusler films, shape memory effect

Received: June 14, 2021

Revised: August 2, 2021

Published online: September 14, 2021

- [1] V. A. Chernenko, E. Cesari, V. V. Kokorin, I. N. Vitenko, *Scr. Metall. Mater.* **1995**, *33*, 1239.
- [2] K. Ullakko, J. K. Huang, C. Kantner, R. C. O'Handley, V. V. Kokorin, *Appl. Phys. Lett.* **1996**, *69*, 1966.
- [3] A. Sozinov, N. Lanska, A. Soroka, W. Zou, *Appl. Phys. Lett.* **2013**, *102*, 021902.
- [4] T. Krenke, E. Duman, M. Acet, E. F. Wassermann, X. Moya, L. Mañosa, A. Planes, *Nat. Mater.* **2005**, *4*, 450.
- [5] V. Srivastava, Y. Song, K. Bhatti, R. D. James, *Adv. Energy Mater.* **2011**, *1*, 97.
- [6] M. Gueltig, F. Wendler, H. Ossmer, M. Ohtsuka, H. Miki, T. Takagi, M. Kohl, *Adv. Energy Mater.* **2017**, *7*, 1601879.
- [7] S. Fabbri, F. Albertini, A. Paoluzi, F. Bolzoni, R. Cabassi, M. Solzi, L. Righi, G. Calestani, *Appl. Phys. Lett.* **2009**, *95*, 022508.
- [8] A. A. Cherechukin, I. E. Dikshtein, D. I. Ermakov, A. V. Glebov, V. V. Koledov, D. A. Kosolapov, V. G. Shavrov, A. A. Tulaiikova, E. P. Krasnoperov, T. Takagi, *Phys. Lett. A* **2001**, *291*, 175.
- [9] S. Stadler, M. Khan, J. Mitchell, N. Ali, A. M. Gomes, I. Dubenko, A. Y. Takeuchi, A. P. Guimarães, *Appl. Phys. Lett.* **2006**, *88*, 192511.
- [10] A. Diestel, R. Niemann, B. Schleicher, S. Schwabe, L. Schultz, S. Fähler, *J. Appl. Phys.* **2015**, *118*, 023908.
- [11] M. Kohl, *Shape Memory Microactuators*, Springer, Berlin **2011**.
- [12] M. Kohl, M. Gueltig, V. Pinneker, R. Yin, F. Wendler, B. Krevet, *Micromachines* **2014**, *5*, 1135.
- [13] G. Jakob, T. Eichhorn, M. Kallmayer, H. J. Elmers, *Phys. Rev. B* **2007**, *76*, 174407.
- [14] H. B. Wang, F. Chen, Z. Y. Gao, W. Cai, L. C. Zhao, *Mater. Sci. Eng., A* **2006**, *438–440*, 990.
- [15] M. Campanini, L. Nasi, S. Fabbri, F. Casoli, F. Celegato, G. Barrera, V. Chiesi, E. Bedogni, C. Magén, V. Grillo, G. Bertoni, L. Righi, P. Tiberto, F. Albertini, *Small* **2018**, *14*, 1803027.
- [16] D. Auernhammer, M. Schmitt, M. Ohtsuka, M. Kohl, *Eur. Phys. J.: Spec. Top.* **2008**, *158*, 249.
- [17] M. Reinhold, D. Kiener, W. B. Knowlton, G. Dehm, P. Müllner, *J. Appl. Phys.* **2009**, *106*, 053906.
- [18] D. Musienko, L. Straka, L. Klimša, A. Saren, A. Sozinov, O. Heczko, K. Ullakko, *Scr. Mater.* **2018**, *150*, 173.
- [19] I. R. Aseguinolaza, V. Golub, O. Y. Salyuk, B. Muntiferung, W. B. Knowlton, P. Müllner, J. M. Barandiarán, V. A. Chernenko, *Acta Mater.* **2016**, *111*, 194.
- [20] N. Baumann, E. Muroto, J. Janek, *Solid State Ionics* **2010**, *181*, 7.
- [21] F. Leroy, Ł. Borowik, F. Cheynis, Y. Almadori, S. Curio, M. Trautmann, J. C. Barbé, P. Müller, *Surf. Sci. Rep.* **2016**, *71*, 391.
- [22] C. V. Thompson, *Annu. Rev. Mater. Res.* **2012**, *42*, 399.
- [23] R. Niemann, A. Backen, S. Kauffmann-Weiss, C. Behler, U. K. Rößler, H. Seiner, O. Heczko, K. Nielsch, L. Schultz, S. Fähler, *Acta Mater.* **2017**, *132*, 327.
- [24] S. Schwabe, R. Niemann, A. Backen, D. Wolf, C. Damm, T. Walter, H. Seiner, O. Heczko, K. Nielsch, S. Fähler, *Adv. Funct. Mater.* **2020**, *31*, 2005715.
- [25] M. Thomas, O. Heczko, J. Buschbeck, U. K. Rößler, J. McCord, N. Scheerbaum, L. Schultz, S. Fähler, *New J. Phys.* **2008**, *10*, 023040.

- [26] N. Teichert, A. Auge, E. Yüzüak, I. Dincer, Y. Elerman, B. Krumme, H. Wende, O. Yildirim, K. Potzger, A. Hütten, *Acta Mater.* **2015**, *86*, 279.
- [27] P. Ranzieri, S. Fabbri, L. Nasi, L. Righi, F. Casoli, V. A. Chernenko, E. Villa, F. Albertini, *Acta Mater.* **2013**, *61*, 263.
- [28] S. Kaufmann, R. Niemann, T. Thersleff, U. K. Rößler, O. Heczko, J. Buschbeck, B. Holzapfel, L. Schultz, S. Fähler, *New J. Phys.* **2011**, *13*, 053029.
- [29] A. Diestel, V. Neu, A. Backen, L. Schultz, S. Fähler, *J. Phys.: Condens. Matter* **2013**, *25*, 266002.
- [30] A. Diestel, A. Backen, U. K. Rößler, L. Schultz, S. Fähler, *Appl. Phys. Lett.* **2011**, *99*, 092512.
- [31] D. Amram, L. Klinger, E. Rabkin, *Acta Mater.* **2012**, *60*, 3047.
- [32] E. Rabkin, D. Amram, E. Alster, *Acta Mater.* **2014**, *74*, 30.
- [33] J. Ye, C. V. Thompson, *Acta Mater.* **2011**, *59*, 582.
- [34] S. G. Wang, E. K. Tian, C. W. Lung, *J. Phys. Chem. Solids* **2000**, *61*, 1295.
- [35] D. C. Dunand, P. Müllner, *Adv. Mater.* **2011**, *23*, 216.
- [36] V. K. Srivastava, S. K. Srivastava, R. Chatterjee, G. Gupta, S. M. Shivprasad, A. K. Nigam, *Appl. Phys. Lett.* **2009**, *95*, 114101.
- [37] W. L. Ling, T. Giessel, K. Thürmer, R. Q. Hwang, N. C. Bartelt, K. F. McCarty, *Surf. Sci.* **2004**, *570*, L297.
- [38] D. J. Srolovitz, M. G. Goldiner, *JOM* **1995**, *47*, 31.
- [39] E. Sutter, P. Sutter, *Nanotechnology* **2006**, *17*, 3724.
- [40] M. S. Kamran, H. Ali, M. Farhan, Y. B. Tang, Y. G. Chen, H. S. Wang, *Int. J. Refrig.* **2016**, *68*, 94.
- [41] J. G. Hust, A. B. Lankford, *Thermal Conductivity of Aluminum, Copper, Iron, and Tungsten for Temperatures from 1 K to the Melting Point*, National Bureau of Standards, Boulder, CO **1984**.
- [42] A. C. Abhyankar, Y. T. Yu, Y. K. Kuo, G. W. Huang, C. S. Lue, *Intermetallics* **2010**, *18*, 2090.
- [43] S. Y. Yu, Z. X. Cao, L. Ma, G. D. Liu, J. L. Chen, G. H. Wu, B. Zhang, X. X. Zhang, *Appl. Phys. Lett.* **2007**, *91*, 102507.
- [44] C. B. Alcock, V. P. Itkin, M. K. Horrigan, *Can. Metall. Q.* **1984**, *23*, 309.
- [45] K. Bhattacharya, *Microstructure of Martensite: Why It Forms and How It Gives Rise to the Shape-Memory Effect*, Oxford University Press, Oxford, UK **2003**.
- [46] F. Khelifaoui, M. Kohl, J. Buschbeck, O. Heczko, S. Fähler, L. Schultz, *Eur. Phys. J.: Spec. Top.* **2008**, *158*, 167.
- [47] I. Horcas, R. Fernández, J. M. Gómez-Rodríguez, J. Colchero, J. Gómez-Herrero, A. M. Baro, *Rev. Sci. Instrum.* **2007**, *78*, 013705.